ARTICLE

J. Cent. South Univ. (2019) 26: 1469−1480
DOI: https://doi.org/10.1007/s11771-019-4103-x

Springer

Synthesis of spherical tremella-like Sb_2O_3 structures derived from metal-organic framworks and its lithium storage properties

TAN Yu-ming(谭玉明), CHEN Xian-hong(陈宪宏), ZHU Yi-rong(朱裔荣), CHEN Li-juan(陈丽娟)

College of Metallurgy and Materials Engineering, Hunan University of Technology, Zhuzhou 412007, China

Abstract: A novel spherical tremella-like Sb_2O_3 was prepared by using metal-organic frameworks (MOFs) method under a mild liquid-phase reaction condition, and was further employed as an anode material for lithium-ion batteries (LIBs). The effect of reaction temperature and time on morphologies of Sb_2O_3 was studied. The results from SEM and TEM demonstrate that the tremella-like Sb_2O_3 architecture are composed of numerous nanosheets with high specific surface area. When the tremella-like Sb_2O_3 was used as LIBs anode, the discharge and charge capacities can achieve 724 and 446 mA·h/g in the first cycle, respectively. Moreover, the electrode retains an impressive high capacity of 275 mA·h/g even after 50 cycles at 20 mA/g, indicating that the material is extremely promising for application in LIBs.

Key words: antimony trioxide; spherical tremella-like structure; metal organic frameworks; anode material; lithium-ion batteries

Cite this article as: TAN Yu-ming, CHEN Xian-hong, ZHU Yi-rong, CHEN Li-juan. Synthesis of spherical tremella-like Sb_2O_3 structures derived from metal-organic framworks and its lithium storage properties [J]. Journal of Central South University, 2019, 26(6): 1469−1480. DOI: https://doi.org/10.1007/s11771-019-4103-x.

1 Introduction

Metal oxide nanomaterials are one of the most important classes of materials due to their excellent properties and wide applications in lithium ion batteries (LIBs) [1−7]. Among diverse metal oxide nanomaterials, the antimony oxide (Sb_2O_3) has been considered as an attractive candidate of electrode material for LIBs, because it can afford a high theoretical specific capacity of 1109 mA·h/g compared with graphite of 372 mA·h/g [6−8]. In recent years, many works have been reported for synthesis of Sb_2O_3 anode material. For instance, ZHOU et al [9] reported that a Sb_2O_3 anode material with nest-shaped architecture exhibited a capacity of 116 mA·h/g after 100 charge/discharge cycles, and only retained 18% of its initial capacity (1081 mA·h/g) owing to the large volume expansion of the Sb_2O_3 material. However, researches on the synthesis of Sb_2O_3 for the anode material in lithium-ion batteries still exist some challenges [10, 11]. The primary challenges related to Sb_2O_3 anodes are the capacity loss and poor cycling performance caused by large volume change and particle pulverization [12, 13]. To address this problem, one possible method is to control the morphologies of Sb_2O_3, which could improve their electrochemical performances such as cycling behavior and rate capability [14, 15]. At present, the different morphologies of Sb_2O_3 have been reported, including nanoparticles [16], nanowires [17], nanorods [17, 18], nanobelts [19], nanoplates [20], octahedral particles [21]. Although

Foundation item: Project(51674114) supported by the National Natural Science Foundation of China; Project(2019JJ40069) supported by the Natural Science Foundation of Hunan Province, China; Project(16K025) supported by the Key Laboratory of the Education Department of Hunan Province, China

Received date: 2018-11-13; **Accepted date:** 2019-04-17

Corresponding author: CHEN Xian-hong, PhD, Professor; Tel: +86-731-22183466; E-mail: xianhongchen@hnu.edu.cn; ORCID: 0000-0002-1747-7222

some efforts had been devoted to synthesize nanostructured Sb_2O_3 with diverse morphologies, the rational design and controllable synthesis of Sb_2O_3 nanostructures with more active sites and more stable structures are still big challenges [22].

Metal-organic frameworks (MOFs), a new class of hybrid functional materials with high porosity, large surface area and chemical tunability, have attracted enormous interest in recent years [23−27]. In general, MOFs have nanosized cavities and open a pathway for small molecules to access and escape, allowing them to behave as sacrificial templates or precursors to be converted into functional nanostructures. Therefore, it has been used as important templates or precursors to synthesize anode materials with unique morphologies and structures which are beneficial to the electrochemical reaction kinetics, the buffer of volume changes and further the electrochemical performance [28]. By taking advantage of their unique morphologies and structures, various porous carbons and metal oxides can be achieved easily derived from MOFs. For example, the microporous carbon polyhedrons were produced through the calcination of Zn-based MOFs (ZIF-8) under an inert atmosphere [29]. ZHANG et al [30] succeeded in the scalable synthesis of hollow Fe_2O_3 microboxes through the simultaneous oxidative decomposition of Prussian blue microcubes and crystal growth of iron oxide shells. While porous hierarchical $NiMn_2O_4$/C tremella-like nanostructures are reported through a simple solvothermal and calcination method [31], revealing a superior specific capacity of 2130 mA·h/g at 350 cycles at a current density of 1 A/g. The porous tremella-like nanostructure provides sufficient contact with electrolyte and fast three-dimensional Li^+ diffusion channels, and dramatically improves the capacity of $NiMn_2O_4$/C via interfacial storage. Nevertheless, the tremella-like Sb_2O_3 for application in LIBs from MOFs has not been reported.

Herein, we report a simple and scalable synthesis of Sb_2O_3 tremella-like structure by using [Sb-MOF] (MOF=2-methylimidazole) as self-sacrificing templates. The as-synthesized Sb_2O_3 is composed of a number of two-dimensional thin nanosheets with high specific surface area. When the tremella-like Sb_2O_3 structure applied as anode materials for LIBs, it shows significantly improved electrochemical performance because the structure can improve the electrode/electrolyte contact area, which makes the diffusion of electrolyte into the inner region of the electrodes easily and eventually accelerates Li-ion diffusion [31−35].

2 Experimental

2.1 Materials

Antimony trichloride ($SbCl_3$) was purchased from Sinopharm Group Chemical Reagent Co., Ltd., and 2-methylimidazole (2MI) was obtained from Aladdin-Shanghai Jingchun Biochemical Technology Co., Ltd. Ethanol (EtOH) and methanol (MeOH) were purchased from Tianjin Fuqi Chemical Co., Ltd. All the reagents were commercially available and were used without further purification.

2.2 Preparation of tremella-like Sb_2O_3

5 mmol $SbCl_3$ was dissolved in 80 mL EtOH/MeOH (V:V=1:1) solution under magnetic stirring, and the mixture solution was placed in a water bath at 30 °C. 20 mmol 2MI was dissolved in another mixture of 40 mL EtOH and 40 mL MeOH under a water bath at 30 °C, then quickly poured above mixture solution into $SbCl_3$ solution. Subsequently, the resulting solution was sealed and kept continuously stirring at 30 °C for 24 h. Finally, the white precipitates were collected by filter, washed several times with abundant EtOH and distilled water, and dried at 50 °C overnight in air. The other samples were prepared at 10 °C and 50 °C, respectively, without changing other conditions.

2.3 Characterization

The crystal phase of the products was examined by X-ray diffraction (XRD, Siemens D5000, Japan) applying Cu K_α radiation (λ= 1.5418 Å) with 2θ range from 10° to 90° at 40 kV. The morphologies and structures of the products were investigated by field emission scanning electron microscopy (FESEM, JEOL JSM-6700F, Tokyo, Japan) with an accelerating voltage of 20 kV and transmission electron microscopy (TEM, JEOL JSM-3010, Tokyo, Japan) with an operating voltage of 200 kV. The composition of samples was analyzed by the energy-dispersive X-ray (EDS) maps attached to the FESEM instrument. The

surface area and pore size distribution of samples were measured by N_2 adsorption-desorption isotherms (BET, Micromeritics ASAP 2020, Mike, American) at 77 K.

2.4 Electrochemical measurements

The working electrodes consisted of 80 wt% of the active material (AM), 10 wt% of acetylene black (AB), and 10 wt% of poly vinylidene chloride (PVDF). The slurry was painted on a copper foil current collector, and were rolled into 30 μm sheets. Then the film was dried at 100 °C for 12 h in a vacuum oven, and cut into disks with a diameter of 14 mm. The solution of 1.0 mol/L $LiPF_6$ in a mixture of ethyl carbonate (EC) and dimethyl carbonate (DMC) (1:1 in volume) was used as the electrolyte. The CR2025-type coin half-cells were assembled in an argon-filled glove box using a lithium foil as the counter electrode and a Celgard 2400 polypropylene membrane as the separator.

The cyclic voltammetry (CV) was tested at a scan rate of 0.1 mV/s in a potential range of 0–3.0 V using a CHI660E electrochemical workstation. The galvanostatic charge-discharge (GSCD), cycling and rating performance was conducted by the NEWARE multi-channel battery testing system at room temperature (25±2) °C between 0.01 and 3.0 V versus Li^+/Li. The electrochemical impedance spectroscopic (EIS) was performed in the range of 100 kHz to 0.1 Hz on CHI660E electrochemical workstation.

3 Results and discussion

3.1 Structural verification

To examine the crystal structure of the prepared materials, XRD was used. Figure 1 shows XRD patterns of the samples prepared at 10, 30 and 50 °C, respectively. It can be observed from Figure 1 that the samples exhibit two types of crystal structures. Figures 1(a) and (b) have similar diffraction peaks at 19.4°, 25.5°, 28.4°, 33.8°, 47.1°, 50.5°, 54.8° and 60.8° corresponding to the crystal planes (110), (111), (121), (012), (240), (161), (170) and (242), respectively. These diffraction peaks are in accordance with JCPDS No. 11-0689, implying that both Figures 1(a) and (b) belong to orthorhombic valentinite of Sb_2O_3. However, the diffraction peaks of Figure 1(c) at 13.7°, 27.7°, 32.1°, 35.0°, 46.0°, 54.5°, 57.2° and 74.0° correspond to the crystal planes (111), (222), (400), (331), (440), (622), (444) and (662), respectively, and can be well matched with the standard peaks of cubic senarmonite of Sb_2O_3 (JCPDS No. 43-1071). The above results manifest that the temperature has a great influence on the formation of crystal structure of Sb_2O_3. As a rule, there is an unequal in the structural verification part of the crystal plane in the crystal growth process under different temperature conditions, and the kinetic effect of the reaction makes the differences of the crystal growth rate of each crystal plane, resulting in a variety of crystal structures and morphologies. At 10 °C and 30 °C, due to the relatively high surface energy of (121) for Sb_2O_3 and a kinetic effect involving a cyclic generation of highly reactive adsorption sites [36, 37], the crystal growth along the (121) facets is dominant compared with other facets. In addition, the sample obtained at 50 °C (Figure 1(c)) can easily find that the maximum diffraction peak corresponds to the crystal planes of (222). It was thought that the growth of the crystal along (222) planes was preferred based on the above same reason. The above results manifest the temperature has a great influence on the formation of different crystal structures of Sb_2O_3.

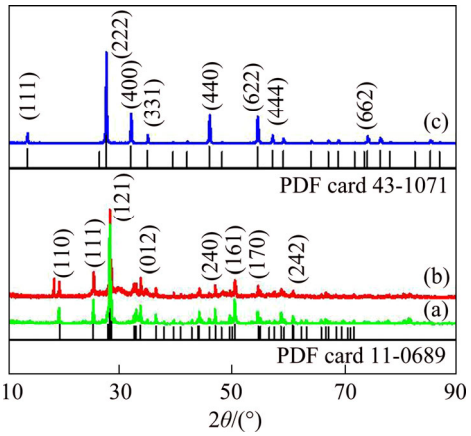

Figure 1 XRD patterns of samples obtained at different temperatures: (a) 10 °C; (b) 30 °C; (c) 50 °C

3.2 Morphology of as-obtained samples

The morphology of the prepared Sb_2O_3 was characterized by FESEM, as shown in Figure 2. When the reaction temperature is 10 °C, it can be observed that the morphology of the as-resulted samples mainly shows the spherical particles (Figure 2(a)), and the diameter of the particles is about 0.5−1 μm. In order to understand the detailed structure of the spherical particles, a further

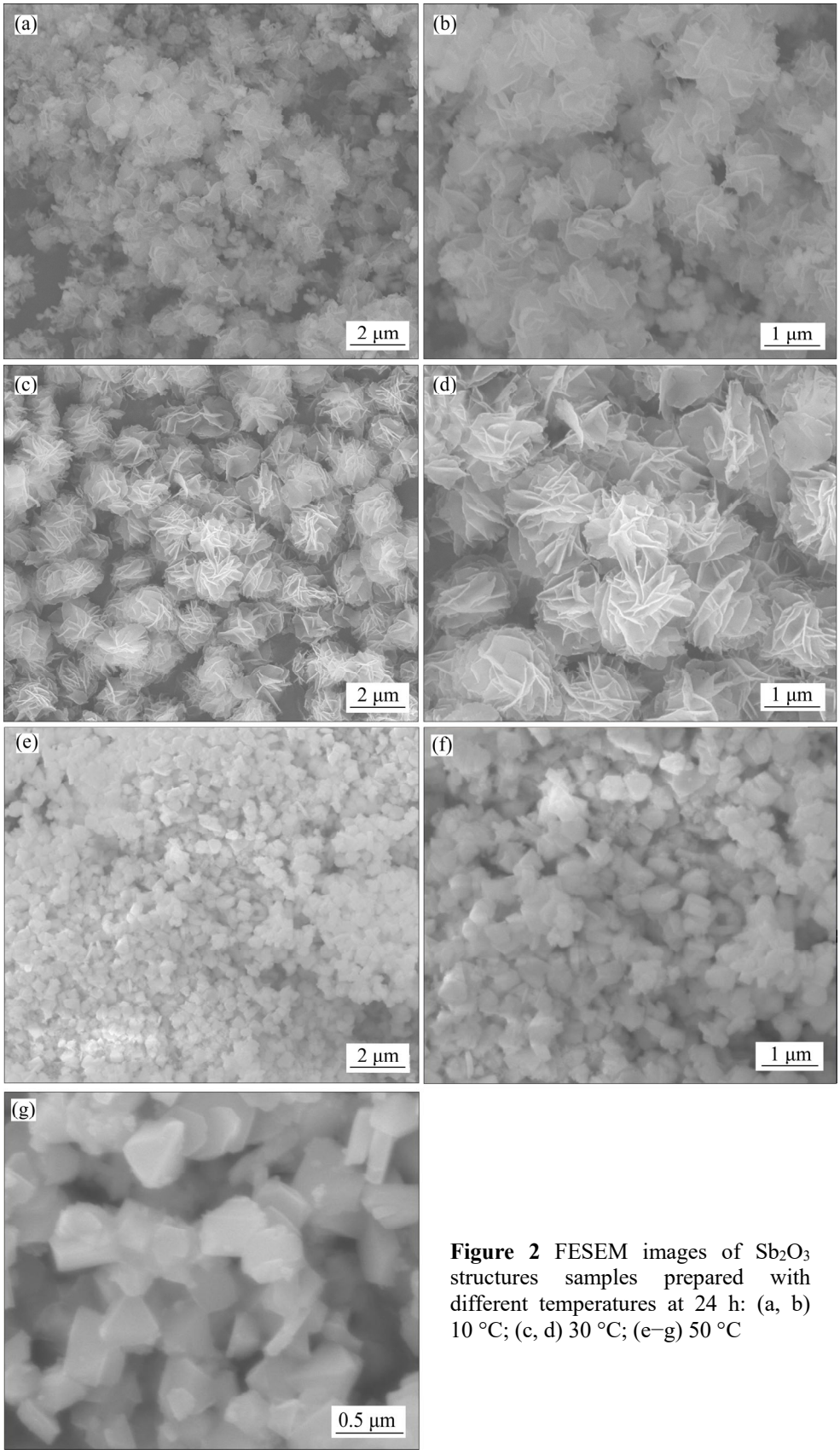

Figure 2 FESEM images of Sb_2O_3 structures samples prepared with different temperatures at 24 h: (a, b) 10 °C; (c, d) 30 °C; (e−g) 50 °C

enlargement is shown in Figure 2(b). It could be found that some wrinkles combined with similar unclear outline nanosheets grow on the surfaces of the partially spherical particles to form a flower-like morphology. The spherical-shaped morphology with high homogeneity is formed when the reaction

temperature is 30 °C (Figure 2(c)). It can be seen that the spherical particles have a diameter about 1.5 μm. Interestingly, it is observed that most of spherical particles are composed of random-shaped nanosheets which possess smooth and clean surfaces (Figure 2(d)). However, the sample obtained at 50 °C (Figure 2(e)) shows a size of 0.5 μm in diameter. Furthermore, a higher magnification SEM image (Figures 2(f)−(g)) discloses that a number of particles are multi-lateral shape, completely different from tremella-shaped structures. These results are also consistent with the XRD analysis in Figure 1. The above results imply that the reaction temperature strongly influences the structure and morphology of the resulting Sb_2O_3 samples.

Recent studies show that the tremella-like structure is beneficial to effectively improve the electrochemical properties due to sufficient contact with electrolyte, decreasing the diffusion distance and accommodating volume changes during charging/discharging processes [31−34]. Therefore, the sample with tremella-like structure (30 °C) was further characterized by EDS, as shown in Figure 3. It can be found from Figures 3(a)−(c) that the Sb and O elements are uniformly distributed over the whole area of the tremella-like structure, indicating a co-existence of Sb and O in the structure. In addition, the EDS spectra of tremella-like (Figure 3(d)) display that the ratio of Sb/O in sample is 0.6118 (Sb:O≈2:3), and also agrees well with the above XRD result.

Furthermore, the tremella-like structural details of as-prepared Sb_2O_3 at 30 °C were further investigated by TEM, as shown in Figure 4. A spherical morphology is observed from Figure 4(a) and the diameter of the sphere is about 1.5 μm. It can be found from Figures 4(b)−(c) (the corresponding magnified marginal images from Figure 4(a)) that the sphere is assembled by nanoplatelets, which are very thin and present slight differential shrinkage. Furthermore, it could be found that the spherical morphology is composed of these nanoplatelets connecting to each other to form some loose space. The lattice fringe of the tremella-like structure (Figure 4(d)) is about 0.3135 nm, corresponding to (121) plane of the orthorhombic valentinite Sb_2O_3 (JCPDS No. 11-0689).

The specific surface areas and pore-size distribution of the Sb_2O_3 structure were examined by N_2 adsorption−desorption measurement. As

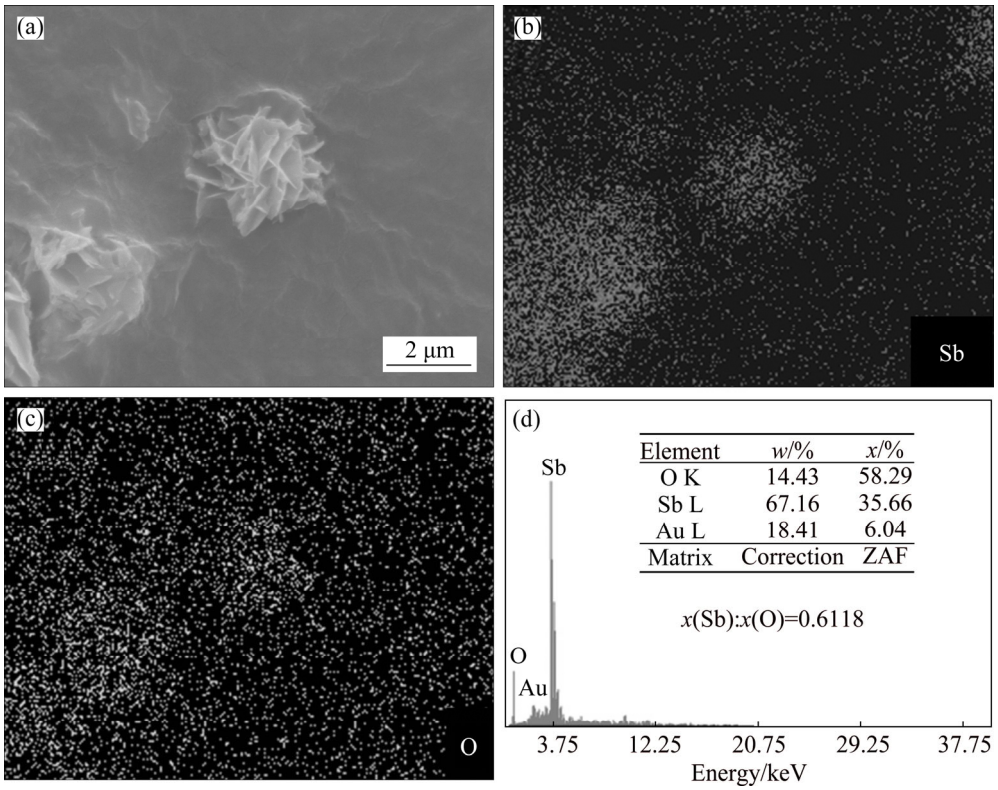

Figure 3 SEM image (a), corresponding EDS-elemental mapping images (b, c), and EDS spectrum (d) of tremella-like structure Sb_2O_3 at 30 °C

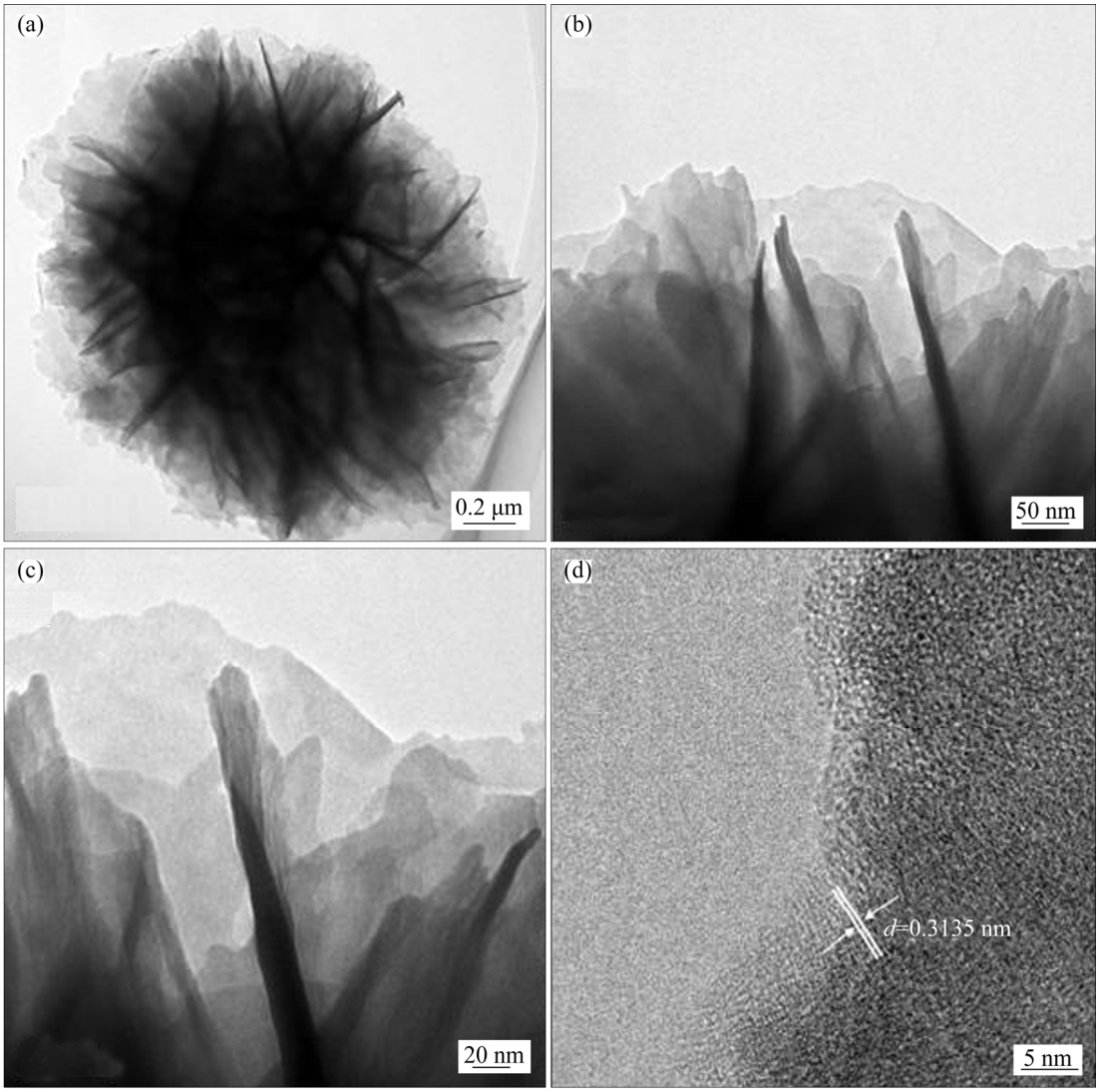

Figure 4 TEM images of tremella-like structure Sb_2O_3 at 30 °C

shown in Figure 5, the isotherm exhibits a typical type IV isotherm with an evident hysteresis loop, showing the mesoporous characteristics of Sb_2O_3. The BET surface areas of tremella-like (30 °C) Sb_2O_3 structure are 971.2 m^2/g, which is much higher than that of the flower-like (10 °C) Sb_2O_3 structure (726.3 m^2/g) and particle-like (50 °C) Sb_2O_3 structure (139.7 m^2/g). The pore size distribution was computed by the Barrett-Joyner-Halenda method based on the adsorption data displaying the average pore size of the flower-like, tremella-like and particle-like Sb_2O_3 at around 8 nm, 29 nm and 7 nm, respectively (the inset of Figure 5). The mesopores may originate from the release of gas molecule and the interspace between adjacent particles. The large surface areas of the tremella-like Sb_2O_3 structure will provide the possibility of efficient transport of electrons and ions. Thus, the lithium storage performance of the tremella-like Sb_2O_3 structure can be improved.

3.3 Influences of time on tremella-like Sb_2O_3 structure

In order to further understand the actual evolutionary process of the tremella-like structure at 30 °C, a series of time-dependent experiments were carried out, and the SEM images of intermediate products obtained by different reaction intervals are shown in Figure 6. At the primary stage (2 h), the as-prepared Sb_2O_3 displays particle morphologies with diameters of 0.5−1 μm (Figure 6(a)). When the reaction time is prolonged to 6 h, similar flower-shaped morphologies assembled by thick sheets with 1.5−2 μm in diameter are found (Figure 6(b)). As the reaction time is further prolonged to 12 h, the majority of

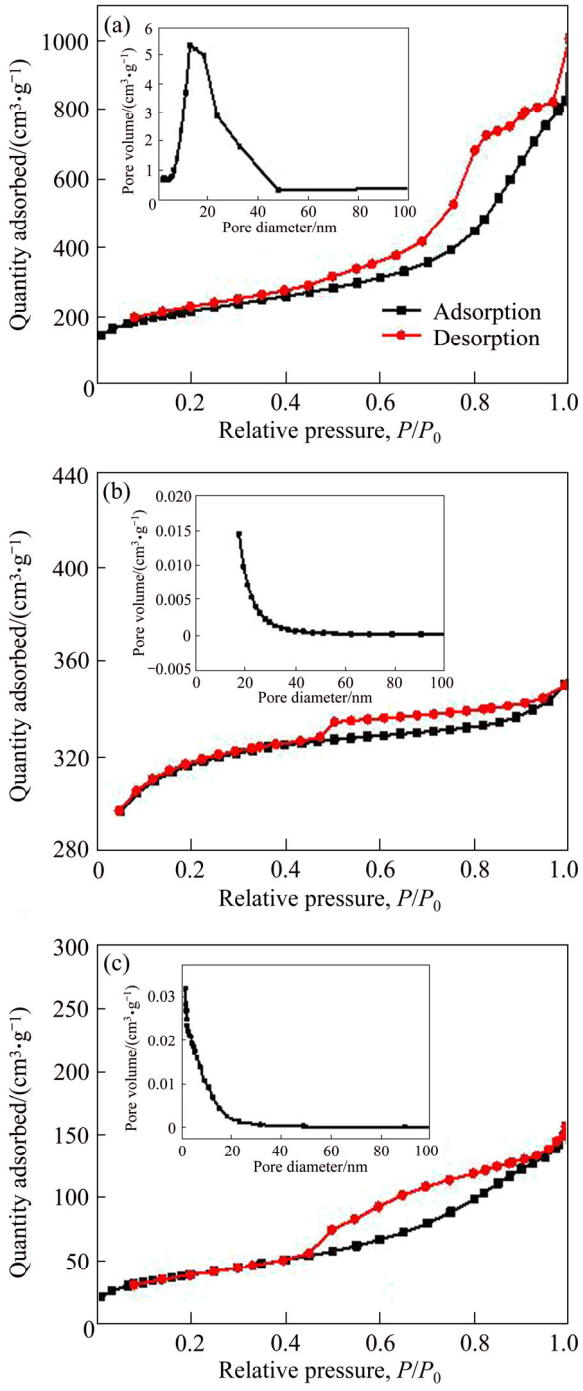

Figure 5 N_2 adsorption−desorption isotherms and pore size distributions (inset) of as-prepared Sb_2O_3: (a) Flower-liked (10 °C); (b) Tremella-liked (30 °C); (c) Particle-liked (50 °C)

tremella-like Sb_2O_3 morphologies (Figure 6(c)) can be observed, meanwhile, some particles are also watched. The diameter of tremella-shape structure is 1.5−2 μm. As the reaction is conducted for 24 h, almost only the tremella-shaped morphologies with the diameter of 1.5−2 μm can be seen from Figure 6(d). It is not difficult to find that tremella-like morphology of the obtained Sb_2O_3 depends strongly on the reaction time. The reaction time is at least 12 h to form the tremella-shaped morphology, and the reaction time is 24 h to form the uniform and perfect tremella-shaped structure.

On the basis of the above experimental results, the formation mechanisms of tremella-like Sb_2O_3 are briefly illustrated in Figure 7. At the first stage, the nuclei of crystal are formed. In the reaction solution, 2-methylimidazole very quickly removes to hydrogen ion and then transforms to an intermediate compound [Sb-MOF] through combining with Sb^{3+} ion [38, 39]. Subsequently, the [Sb-MOF] would further grow along the initial nuclei, and the [Sb-MOF] nanoparticles were formed with reaction time. And then, the freshly crystalline nanoparticles were unstable because of their high surface energy. They tended to aggregate and grow into inhomogeneous ultrathin nanoplatekets (or nanoflakes), driven by the minimization of interfacial energy. Such ultrathin nanoplatekets would self-assemble into hierarchical architecture to minimize the surface energy [32, 40]. Finally, the 3D hierarchical tremella-like Sb_2O_3 could be obtained due to Ostwald ripening after the air oxidation in a drying oven at 50 °C [40].

3.4 Electrochemical performances

The electrochemical properties of the Sb_2O_3 were measured by CV, galvanostatic discharge−charge cycling experiments and EIS experiments. Figure 8(a) shows the CV curve of tremella-liked (30 °C) at a scan rate of 0.1 mV/s over the voltage range of 0.001−3.0 V. A reduction peak appears at 1.48 V, which corresponds to the initial reduction of Sb_2O_3 to Sb and the formation of Li_2O [9, 41]. There is an intense peak at around 0.76 V in the discharge process, which is ascribed to the formation of Li_3Sb in the Li-insertion process and the presence of solid electrolyte interface (SEI) [9, 16]. Meanwhile, the oxide peaks are at about 1.15 V and 1.42 V in the charge process, which is assigned to Li-deintercalation process and the oxidation of metallic Sb to Sb_2O_3, respectively [9, 42].

Figure 8(b) displays the discharge−charge curves of the prepared Sb_2O_3 at 10 °C, 30 °C and 50 °C (marked as Sb_2O_3-10, Sb_2O_3-30, Sb_2O_3-50, respectively) at current density of 20 mA/g. It shows that the discharge capacities of the Sb_2O_3-10,

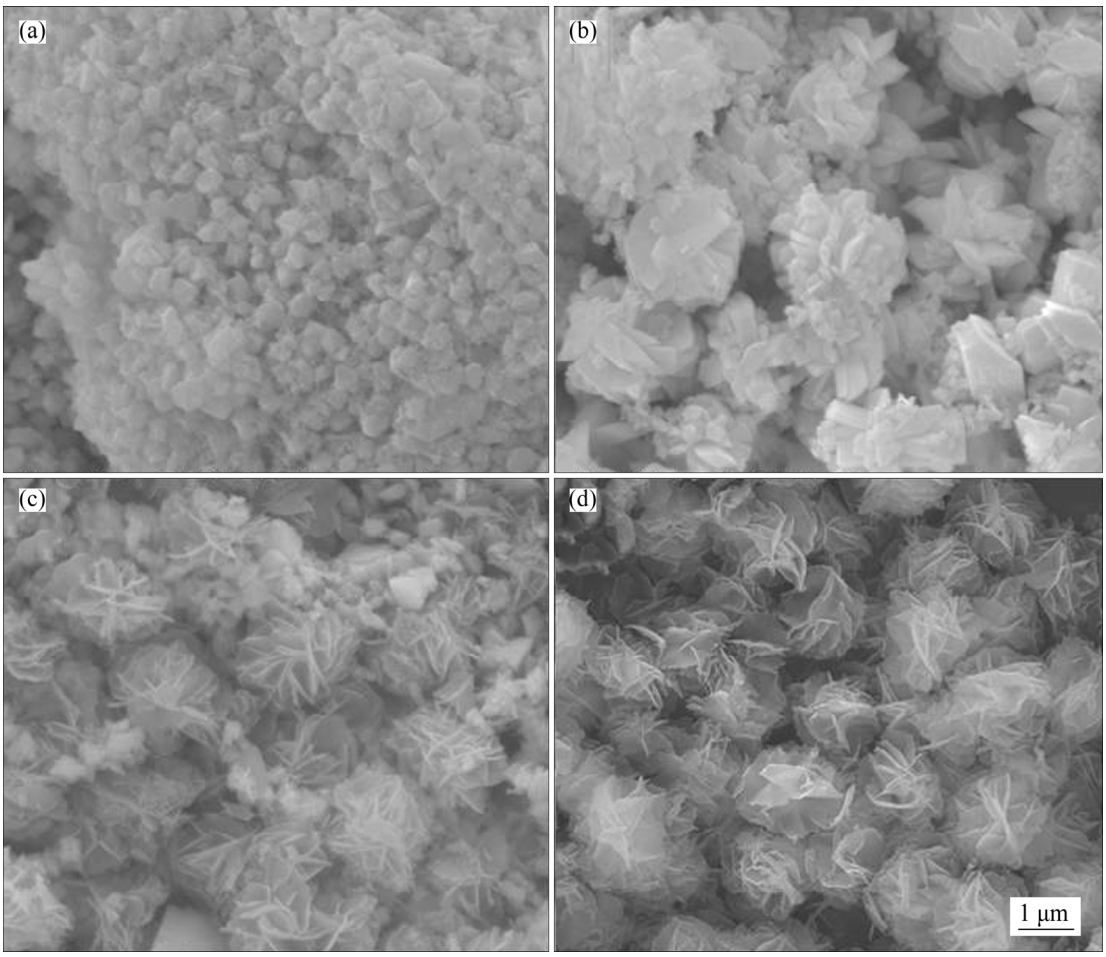

Figure 6 FESEM images of morphology evolution of Sb_2O_3 structures with different reaction time at 30 °C: (a) 2 h; (b) 6 h; (c) 12 h; (d) 24 h

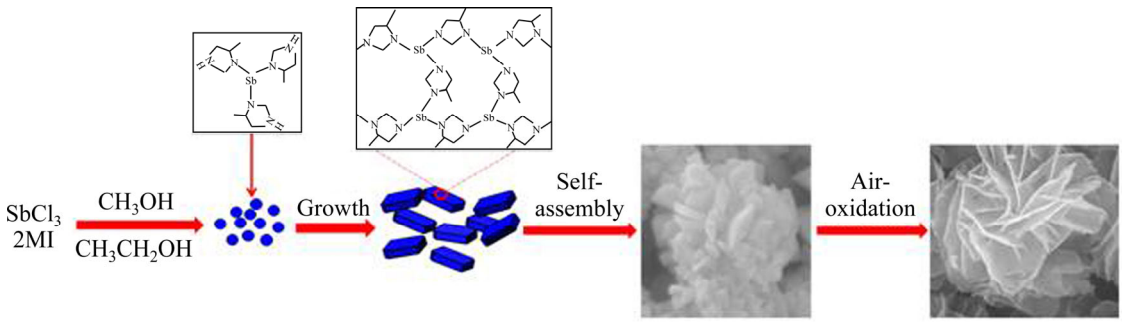

Figure 7 Illustration of preparation processes and formation of tremella-like Sb_2O_3 structure

Sb_2O_3-30, Sb_2O_3-50 are 627, 724 and 559 mA·h/g, and the charge capacities are 276, 446, and 228 mA·h/g, respectively. The corresponding coulombic efficiency (CE) of the three samples are 44.0%, 61.6% and 40.8%, respectively. The cycling performances of Sb_2O_3-10, Sb_2O_3-30 and Sb_2O_3-50 electrodes at 20 mA/g are shown in Figure 8(c). The Sb_2O_3-10, Sb_2O_3-30 and Sb_2O_3-50 electrodes can retain a reversible capacity of 183, 275 and 123 mA·h/g after 50 cycles, respectively. It can be found that the Sb_2O_3-30 electrode is more stable than the other electrodes. In addition, the IE of Sb_2O_3-30 electrodes at 50 cycles is calculated and shown in Figure 8(c) (green line). In the initial few cycles, the Sb_2O_3-30 electrodes have a poor initial coulombic efficiency which may be attributed to the formation of SEI layers at the electrolyte interface, the decomposition of the electrolyte and the reduction of adsorbed impurities on Sb_2O_3 electrode surface [43, 44]. In contrast, the cycling

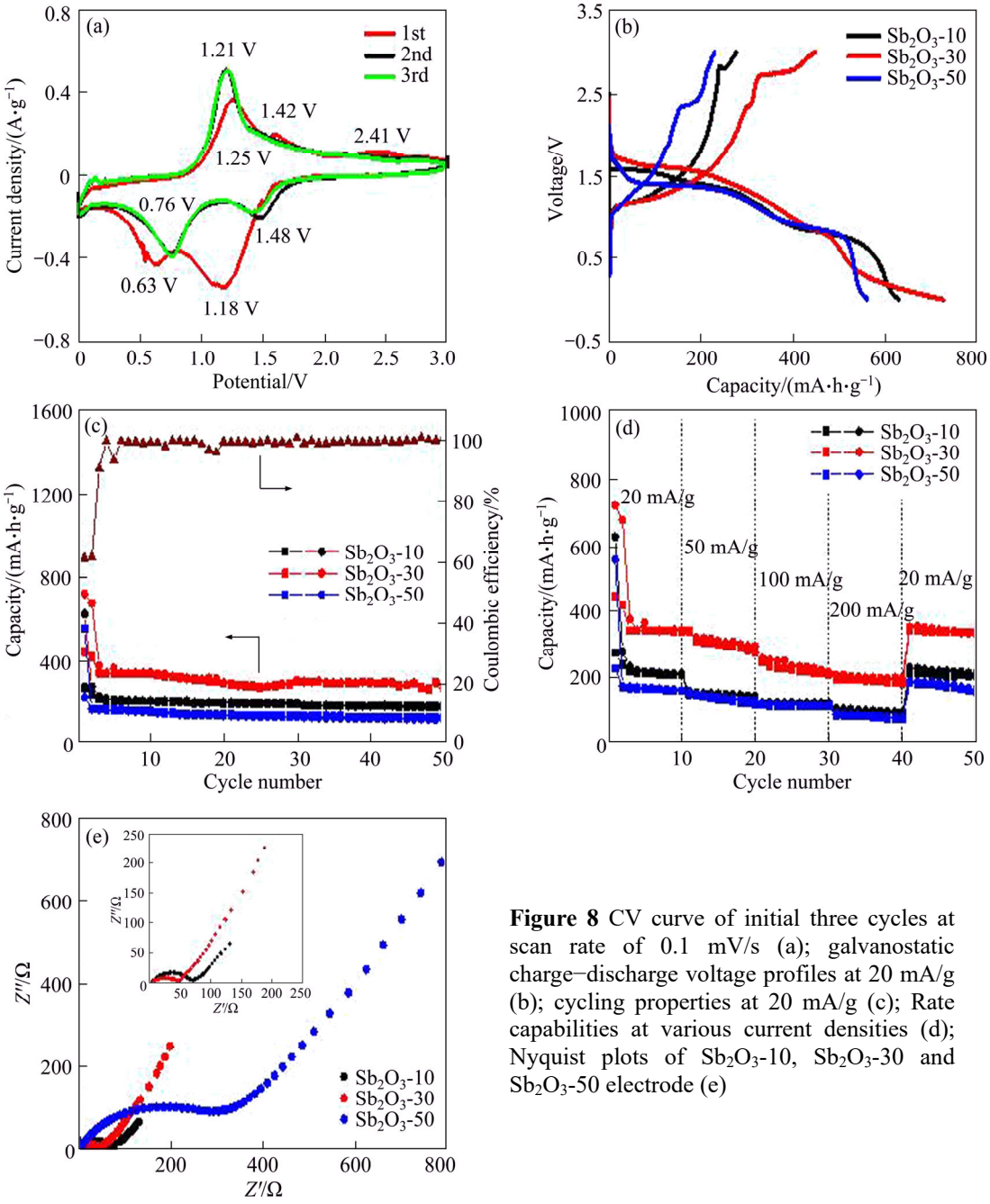

Figure 8 CV curve of initial three cycles at scan rate of 0.1 mV/s (a); galvanostatic charge−discharge voltage profiles at 20 mA/g (b); cycling properties at 20 mA/g (c); Rate capabilities at various current densities (d); Nyquist plots of Sb_2O_3-10, Sb_2O_3-30 and Sb_2O_3-50 electrode (e)

performance of the Sb_2O_3-30 electrode is much better than those of Sb_2O_3 electrodes. The rate performance was measured at different current densities from 20 to 200 mA/g, as shown in Figure 8(d). It can be found that at current densities of 20, 50, 100 and 200 mA/g, the Sb_2O_3-30 delivers the charge capacities of 342, 311, 234 and 200 mA·h/g, respectively, and the rate capacity of the Sb_2O_3-30 electrode is much higher than that of the other electrodes (Sb_2O_3-10 and Sb_2O_3-50). This also means that the tremella-like Sb_2O_3 electrode is more stable than that of the other electrodes. It can be easily concluded that the Sb_2O_3-30 electrode exhibits better electrochemical performance than the Sb_2O_3-10 electrode and Sb_2O_3-50 electrode. It is attributed to the large specific surface area of the tremella-like Sb_2O_3 structures, which increases the active sites of the surface and the edge to accelerate the penetration of lithium ion and electrolyte [31−34].

To verify the electrical conductivity of the Sb_2O_3-10, Sb_2O_3-30 and Sb_2O_3-50, the electrochemical impedance spectroscopy (EIS) measurements were carried out. As shown in Figure 8(e), the Nyquist plots are composed of a semicircle in the high frequencies and an inclined

line at low frequencies. The diameter of the semicircle is assigned to the interfacial charge transfer impedance (R_{ct}) between electrolyte and electrode, while the inclined line is attributed to the Li-ion diffusion process [45, 46]. The R_{ct} values of the Sb_2O_3-10, the Sb_2O_3-30 and the Sb_2O_3-50 electrodes were 71.73, 48.38 and 293.6 Ω, respectively. The Sb_2O_3-30 electrode shows a minimum resistance compared with Sb_2O_3-10 and Sb_2O_3-50 electrodes, indicating that the tremella-like structures are beneficial to enhance charge transfer and diffusion of electrolyte, and can effectively improve the electrical conductivity [47, 48]. The tremella-like structure composed of thin nanosheets can effectively enhance the electrochemical lithium storage activity, which benefits the achievement of highly reversible lithium storage based on a high specific surface area of the tremella-like Sb_2O_3 [31, 32], leading to such a superior performance used in LIBs.

4 Conclusions

In this work, the Sb_2O_3 for anode material of lithium ion battery was prepared from a derivative of metal organic framework by liquid-phase reaction process. Reaction temperature and time have important influences on morphology of Sb_2O_3, leading to a considerable difference in their electrochemical performances. Particularly, the spherical tremella-like Sb_2O_3 structure synthesized at 30 °C for 24 h possesses a diameter of about 1.5 μm. When the tremella-like architecture used as an anode material of LIBs, the discharge and charge capacity can achieve 724 and 446 mA·h/g in the first cycle, respectively, and the initial coulombic efficiency is 61.6%. The charge capacity retains 275 mA·h/g after 50 cycles at 20 mA/g. The tremella-like Sb_2O_3 exhibits enhanced specific capacity, excellent cycling performance, compared with other structures such as particles, rods and plates. Furthermore, this morphology is beneficial to improve the diffusion rate of lithium ions in LIBs. It is not hard to find that the spherical tremella-like Sb_2O_3 are potential anode materials in lithium-ion batteries.

References

[1] JI Li-wen, LIN Zhan, ALCOUTLABI M, ZHANG Xiang-wu. Recent developments in nanostructured anode materials for rechargeable lithium-ion batteries [J]. Energy Environmental Science, 2011, 4(8): 2682−2699.

[2] WU Hao-bin, CHEN Jun-song, HNG Huey-hoon, LOU Xiong-wen. Nanostructured metal oxide-based materials as advanced anodes for lithium-ion batteries [J]. Nanoscale, 2012, 4(8): 2526−2542.

[3] SHI Chong-fu, XIANG Kai-xiong, ZHU Yi-rong, CHEN Xian-hong, ZHOU Wei, CHEN Han. Preparation and electrochemical properties of nanocable-like Nb_2O_5/ surface-modified carbon nanotubes composites for anode materials in lithium ion batteries [J]. Electrochimecal Acta, 2017, 246: 1088−1096.

[4] LONG Zhao-hui, DING Jing, DENG Bo-hua, GONG Jin, LI Xiao-bo, YIN Fu-cheng. First-principle study of Li-insertion properties of $NiSi_2$ as anode materials for lithium-ion batteries [J]. Journal of Central South University, 2018, 49(2): 323−329.

[5] ZHOU Hong-ming, GENG Wen-jun, LI Jian. LiPF6 and lithium difluoro (oxalato) borate/ethylene carbonate+ dimethyl carbonate+ethyl (methyl) carbonate electrolyte for $LiNi_{0.5}Mn_{1.5}O_4$ cathode [J]. Journal of Central South University, 2017, 24: 1013−1018.

[6] LI N, LIAO S, SUN Y, SONG H W, WANG C X. Uniformly dispersed self-assembled growth of Sb_2O_3/Sb@graphene nanocomposites on a 3D carbon sheet network for high Na-storage capacity and excellent stability [J]. Journal of Materials Chemistry A, 2015, 3(11): 5820−5828.

[7] NAM D G, HONG K S, LIM S J, KIM M J, KWON H S. High-performance Sb/Sb_2O_3 anode materials using a polypyrrole nanowire network for Na-ion batteries [J]. Small, 2015,11(24): 2885−2892.

[8] WU Feng-dan, WANG Yong, TANG Jun-jun. Microwave-assisted synthesis of antimony oxide nanostructures and their electrochemical properties [J]. Materials Science Forum, 2010, 650: 157−162.

[9] ZHOU Jing, ZHENG Cai-hong, WANG Hua, YANG Jie, HU Peng-fei, GUO Lin. 3D nest-shaped Sb_2O_3/RGO composite based high-performance lithium-ion batteries [J]. Nanoscale, 2016, 8(39): 17131−17135.

[10] ZHOU Xiao-si, LIU Xia, XU Yan, LIU Yun-xia, DAI Zhi-hui, BAO Jian-chun. An SbO_x/reduced graphene oxide composite as a high-rate anode material for sodium-ion batteries [J]. Journal of Physical Chemistry C, 2014, 118(41): 23527−23534.

[11] XUE Ming-zhe, FU Zheng-wen. Electrochemical reaction of lithium with nanostructured thin film of antimony trioxide [J]. Electrochemical Communications, 2006, 8(8): 1250−1256.

[12] SIMONIN L, LAFONT U, TABRIZI N, SCHMIDT-OTT A, KELDER E-M. Sb/O nano-composites produced via spark discharge generation for Li-ion battery anodes [J]. Journal Power Sources, 2007, 174(2): 805−809.

[13] ZHOU Xiao-zhong, ZHANG Zheng-feng, XU Xiao-hu, YAN Jian, MA Guo-fu, LEI Zi-qiang. Anchoring Sb_6O_{13} nanocrystals on graphene sheets for enhanced lithium storage [J]. ACS Applied Materials Interfaces, 2016, 8(51): 35398−35406.

[14] HE Meng, KRAVCHYK K, WALTER M, KOVALENKO M V. Antimony nanocrystals for high-rate Li-ion and Na-ion

battery anodes: Nano versus bulk [J]. Nano Letters, 2014, 14(3): 1255−1262.

[15] HU Xing-yun, KONG Ling-hao, HE Meng-chang. Kinetics and mechanism of photopromoted oxidative dissolution of antimony trioxide [J]. Environment Science Technology, 2014, 48(24): 14266−14272.

[16] BRYNGELSSON H, ESKHULT J, NYHOLM L, HERRANEN M, ALM O, EDSTRÖM K. Electrodeposited Sb and Sb/Sb_2O_3 nanoparticle coatings as anode materials for Li-ion batteries [J]. Chemistry of Materials, 2007, 19(5): 1170−1180.

[17] DENG Zheng-tao, CHEN Dong, TANG Fang-qiong, MENG Xian-wei, REN Jun, ZHANG Lin. Orientated attachment assisted self-assembly of Sb_2O_3 nanorods and nanowires: End-to-end versus side-by-side [J]. Journal of Physical Chemistry C, 2007, 111(14): 5325−5330.

[18] WANG Gui-zhi, FENG Jian-min, DONG Lei, LI Xi-fei, LI De-jun. Antimony (IV) oxide nanorods/reduced graphene oxide as the anode material of sodium-ion batteries with excellent electrochemical performance [J]. Electrochimistry Acta, 2017, 240: 203−214.

[19] LI Bin-jie, XU Xiang-min, ZHAO Yan-bao, ZHANG Zhi-jun. Fabrication of Sb_2O_3 nanobelt bundles via a facile ultrasound-assisted room temperature liquid phase chemical route and evaluation of their optical properties [J]. Materials Research Bulletin, 2013, 48(3): 1281−1287.

[20] LI Wei, WANG Kang-li, CHENG Shi-jie, JIANG Kai. A two-dimensional hybrid of SbO_x nanoplates encapsulated by carbon flakes as a high performance sodium storage anode [J]. Journal of Materials Chemistry A, 2017, 5(3): 1160−1167.

[21] DENG Ming-xiang, LI Si-jie, HONG Wan-wan, JIANG Yun-ling, XU Wei, SHUAI Hong-lei, ZOU Guo-qiang, HU Yun-chu, HOU Hong-shuai, WANG Wen-lei, JI Xiao-bo. Octahedral Sb_2O_3 as high-performance anode for lithium and sodium storage [J]. Materials Chemistry and Physics, 2019, 223: 46−52

[22] KIBSGAARD J, CHEN Zhe-bo, REINECKE B N, JARAMILLO T F. Engineering the surface structure of MoS_2 to preferentially expose active edge sites for electrocatalysis [J]. Nature Materials, 2012, 11(11): 963−969.

[23] WU Ren-bing, QIAN Xu-kun, YU Feng, LIU Hai, ZHOU Kun, WEI Jun, HUANG Yi-zhong. MOF-templated formation of porous CuO hollow octahedra for lithium-ion battery anode materials [J]. Journal of Materials Chemistry A, 2013, 1: 11126−11129.

[24] SO MONICA C, WIEDERRECHT G P, MONDLOCH J E, HUPP J T, FARHA O K. Metal-organic framework materials for light-harvesting and energy transfer [J]. Chemical Communications, 2015, 51(17): 3501−3510.

[25] TAN Yu-ming, CHEN Li-juan, CHEN Han, HOU Qing-lin, CHEN Xian-hong. Synthesis of a symmetric bundle-shaped Sb_2O_3 and its application for anode materials in lithium ion batteries [J]. Materials Letters, 2018, 212: 103−106.

[26] WANG Lu, HAN Yu-zhen, FENG Xiao, ZHOU Jun-wen, QI Peng-fei, WANG Bo. Metal-organic frameworks for energy storage: Batteries and supercapacitors [J]. Coordination Chemistry Reviews, 2016, 307: 361−381.

[27] HE Han-na, HUANG Dan, TANG You-gen, WANG Qi, JI Xiao-bo, WANG Hai-yan, GUO Zai-ping. Tuning nitrogen species in three-dimensional porous carbon via phosphorus doping for ultra-fast potassium storage [J]. Nano Energy, 2019, 57: 728−736.

[28] DONG Shi-hua, LI Cai-xia, GE Xiao-li, LI Zhao-qiang, MIAO Xian-guang, YIN Long-wei. ZnS-Sb_2S_3@C core-double shell polyhedron structure derived from metal-organic framework as anodes for high performance sodium ion batteries [J]. ACS Nano, 2017, 11(6): 6474−6482.

[29] ZHU Zhi-qiang, WANG Shi-wen, DU Jing, JIN Qi, ZHANG Tian-ran, CHENG Fang-yi, CHEN Jun. Ultrasmall Sn nanoparticles embedded in nitrogen-doped porous carbon as high-performance anode for lithium-ion batteries [J]. Nano Letters, 2013, 14(1): 153−157.

[30] ZHANG Lei, WU Hao-bin, MADHAVI S, HNG H H, LOU Xiong-wen (David). Formation of Fe_2O_3 microboxes with hierarchical shell structures from metal−organic frameworks and their lithium storage properties [J]. Journal of the American Chemical Society, 2012, 134: 17388−17391.

[31] KANG Wen-pei, TANG Yong-bing, LI Wen-yue, YANG Xia, XUE Hong-tao, YANG Qing-dan, LEE Chun-sing. High interfacial storage capability of porous $NiMn_2O_4$/C hierarchical tremella-like nanostructures as the lithium ion battery anode [J]. Nanoscale, 2015, 7(1): 225−231.

[32] LIU Hai-yan, ZHANG Wei, SONG Huai-he, CHEN Xiao-hong, ZHOU Ji-sheng, MA Zhao-kun. Tremella-like graphene/polyaniline spherical electrode material for supercapacitors [J]. Electrochimistry Acta, 2014, 146: 511−517.

[33] WANG Qian, YAN Jun, WANG Yan-bo, WEI Tong, ZHANG Mi-lin, JING Xiao-yan, FAN Zhuang-jun. Three-dimensional flower-like and hierarchical porous carbon materials as high-rate performance electrodes for supercapacitors [J]. Carbon, 2014, 67(2): 119−127.

[34] LIU Hui, ZHANG Fan, LI Wen-yue, ZHANG Xiao-long, LEE Chun-sing, WANG Wen-lou, TANG Yong-bing. Porous tremella-like MoS_2/polyaniline hybrid composite with enhanced performance for lithium-ion battery anodes [J]. Electrochimistry Acta, 2015, 167: 132−138.

[35] ZHANG Rui, LI Hui-yong, SUN Dan, LUAN Jing-yi, HUANG Xiao-bing, TANG You-gen, WANG Hai-yan. Facile preparation of robust porous MoS_2/C nanosheet networks as anode material for sodium ion batteries [J]. Journal of Materials Science, 2019, 54(3): 2472−2482.

[36] ZENG H C. Vapour phase growth of orthorhombic molybdenum trioxide crystals at normal pressure of purified air [J]. Journal of Crystal Growth,1998, 186: 393−402.

[37] ZHANG Zao-li, GUO Lin, WANG Wen-dong. Synthesis and characterization of antimony oxide nanoparticles [J]. Journal of Materials Research, 2001, 16(3): 803−805.

[38] WU Ren-bing, QIAN Xu-kun, RUI Xian-hong, LIU Hai, YADIAN Bo-luo, ZHOU Kun, WEI Jun, YAN Qing-yu, FENG Xi-qiao, LONG Yi, WANG Liu-ying, HUANG Yi-zhong. Zeolitic imidazolate framework 67-derived high symmetric porous Co_3O_4 hollow dodecahedra with highly enhanced lithium storage capability [J]. Small, 2014, 10(10): 1932−1938.

[39] PHAN A, DOONAN C J, URIBE-ROMO F J, KNOBLER C B, O'KEEFFE M, YAGHI O M. Synthesis, structure, and

carbon dioxide capture properties of zeolitic imidazolate frameworks [J]. Accounts of Chemical Research, 2010, 43(1): 58−67.

[40] HU Ling-ling, QU Bai-hua, CHEN Li-bao, LI Qiu-hong. Low-temperature preparation of ultrathin nanoflakes assembled tremella-like NiO hierarchical nanostructures for high-performance lithium-ion batteries [J]. Materials Letters, 2013, 108: 92−95.

[41] YI Zheng, HAN Qi-gang, LI Xiang, WU Yao-ming, CHENG Yong, WANG Li-min. Two-step oxidation of bulk Sb to one-dimensional Sb_2O_4 submicron-tubes as advanced anode materials for lithium-ion and sodium-ion batteries [J]. Chemical Engineering Journal, 2017, 315: 101−107.

[42] ZHOU Xiao-zhong, ZHANG Zheng-feng, LU Xiao-fang, LV Xue-yan, MA Guo-fu, WANG Qing-tao, LEI Zi-qiang. Sb_2O_3 nanoparticles anchored on graphene sheets via alcohol dissolution-reprecipitation method for excellent lithium storage properties [J]. ACS Applied Materials Interfaces, 2017, 9: 34927−34936.

[43] SUN Qian, REN Qin-qi, LI Hong, FU Zheng-wen. High capacity Sb_2O_4 thin film electrodes for rechargeable sodium battery [J]. Electrochemistry Communications, 2011, 13(12): 1462−1464.

[44] LV Hai-long, QIU Song, LU Gui-xia, FU Ya, LI Xiao-yu, HU Chen-xi, LIU Jiu-rong. Nanostructured antimony/carbon composite fibers as anode material for lithium-ion battery [J]. Electrochimistry Acta,2015, 151: 214−221.

[45] ZHOU Xiao-zhong, ZHANG Zheng-feng, WANG Jian-wen, WANG Qing-tao, MA Guo-fu, LEI Zi-qiang. Sb_2O_4/reduced graphene oxide composite as high-performance anode material for lithium ion batteries [J]. Journal of Alloys and Compounds, 2017, 699: 611−618.

[46] HU Ling-yun, ZHU Xiao-shu, DU Yi-chen, LI Ya-fei, ZHOU Xiao-si, BAO Jian-chun. A chemically coupled antimony/multilayer graphene hybrid as a high-performance anode for sodium-ion batteries [J]. Chemistry of Materials, 2015, 27(23): 8138−8145.

[47] HOU Hong-shuai, JING Ming-jun, YANG Ying-chang, ZHU Yi-rong, FANG Lai-bing, SONG Wei-xin, PAN Cheng-chi, YANG Xu-ming, JI Xiao-bo. Sodium/lithium storage behavior of antimony hollow nanospheres for rechargeable batteries [J]. ACS Applied Materials Interfaces, 2014, 6(18): 16189−16196.

[48] ZHANG Yan-dong, XIE Jian, ZHU Tie-jun, CAO Gao-shao, ZHAO Xin-bing, ZHANG Shi-chao. Activation of electrochemical lithium and sodium storage of nanocrystalline antimony by anchoring on graphene via a facile in situ solvothermal route [J]. Journal of Power Sources, 2014, 247(3): 204−212.

(Edited by FANG Jing-hua)

中文导读

MOF 衍生的球形银耳状 Sb_2O_3 结构的合成及其储锂性能

摘要：在液相反应条件下通过 MOFs 制备了一种新颖的球形银耳状的 Sb_2O_3 材料，并将其用作锂离子电池(LIBs)的负极材料。探究了反应温度和时间对 Sb_2O_3 形貌的影响，通过 SEM 和 TEM 的结果表明，银耳状 Sb_2O_3 结构是由许多具有高比表面积的纳米片组成。当银耳状 Sb_2O_3 用作 LIBs 负极时，首次放电和充电容量分别达到 724 和 446 mA·h/g。在 20 mA/g 的电流密度下循环 50 圈后，电极仍保持 275 mA·h/g 的高容量，因此该材料极有希望应用于 LIBs。

关键词：三氧化二锑；球形银耳状结构；金属有机框架材料；负极材料；锂离子电池